RSC Advances

PAPER

View Article Online
View Journal | View Issue

Cite this: *RSC Adv.*, 2026, **16**, 11

Simultaneous synthesis of hydroxyapatite/chitosan composite from crab shells and its polycaprolactone-blended scaffolds for enhanced bone regeneration

Hien Y Hoang, [ab] Hoang Thanh Ngan Hue Nguyen,[c] Bich Dung Mai,[d] Vy Anh Tran,[e] Van Dat Doan [*f] and Van Thuan Le [*ab]

Although the hydroxyapatite–chitosan reinforced poly(ε-caprolactone) composite (PCL/HA–CS) is vital for bone regeneration, it is still predominantly synthesized from various non-biological sources, while natural bioresources, such as crab shell, containing essential precursors, are discarded as waste, causing environmental pollution. Here, we present a sustainable strategy to fabricate bone scaffolds by directly converting crab shells into a HA–CS composite *via* a one-pot process, followed by blending with PCL. The resulting HA–CS composite, containing 78.37% nano-sized HA, exhibited strong antibacterial activity without cytotoxic effects, with minimum inhibitory concentrations of 2.5 mg mL^{-1} and 5 mg mL^{-1} for *S. aureus* and *E. coli*, respectively, and corresponding minimum bactericidal concentrations of 5 mg mL^{-1} and 10 mg mL^{-1}. When combined with PCL, the biogenic material demonstrated balanced mechanical strength, biocompatibility, and excellent mineralization under *in vitro* conditions. A formation mechanism was also proposed, in which the amine groups of CS interact with HA, while residual hydroxyl groups form interfacial bonds with PCL, enabling uniform distribution of HA–CS within the polymer matrix. Moreover, the biodegradation rate (ν) of PCL/HA–CS during the first four weeks could be linearly tuned by adjusting the HA–CS content, following a linear relationship: ν (%/day) = 0.0108 [HA–CS] (%) + 0.1133. This controllability enables better synchronization between scaffold degradation and new bone formation, addressing a major limitation of conventional PCL-based scaffolds. Overall, crab shell waste offers a promising and eco-friendly route to generate high-performance scaffolds for bone tissue engineering.

Received 7th November 2025
Accepted 12th December 2025

DOI: 10.1039/d5ra08574h

rsc.li/rsc-advances

1 Introduction

Bone tissue possesses a remarkable capacity for self-repair; however, large and critical-sized defects caused by trauma, infection, or tumor resection often exceed its natural regenerative ability and require clinical intervention.[1] Conventional approaches such as autografts and allografts are considered the gold standard, yet they suffer from significant drawbacks, including donor-site morbidity, limited supply, and the risk of immune rejection or disease transmission. Consequently, the development of synthetic bone graft substitutes and scaffolds with high biocompatibility, bioactivity, and appropriate mechanical properties has become a key focus in regenerative medicine. Among these, calcium phosphate-based biomaterials, particularly hydroxyapatite (HA), have attracted widespread attention due to their close chemical similarity to the mineral phase of natural bone and their osteoconductive potential.[2,3] Nevertheless, the inherent brittleness, low mechanical strength, and lack of antibacterial properties of HA often limit its use as a standalone scaffold material, especially for applications requiring mechanical resilience, such as orthopaedic implants. To address this limitation, HA is commonly blended with natural polymers, most typically with chitosan (CS).[4,5] CS, derived from the deacetylation of chitin, offers several advantages, including biodegradability, biocompatibility, antibacterial activity, and the ability to promote cell adhesion and proliferation.[6] The successful co-assembly of HA and CS resulted in the formation of a synergistic composite that

[a]*Center for Advanced Chemistry, Institute of Research & Development, Duy Tan University, 03 Quang Trung, Da Nang City, 550000, Vietnam*

[b]*Faculty of Natural Sciences, Duy Tan University, 03 Quang Trung, Da Nang City, 550000, Vietnam. E-mail: levanthuan3@duytan.edu.vn*

[c]*Faculty of Medicine, Duy Tan University, 03 Quang Trung, Da Nang City, 550000, Vietnam*

[d]*Institute of Biotechnology and Food Technology, Industrial University of Ho Chi Minh City, Ho Chi Minh City, 700000, Vietnam*

[e]*Faculty of Applied Science and Technology, Nguyen Tat Thanh University, Ho Chi Minh City, 700000, Vietnam*

[f]*Faculty of Chemical Engineering, Industrial University of Ho Chi Minh City, Ho Chi Minh City, 700000, Vietnam. E-mail: doanvandat@iuh.edu.vn*

combines structural integrity with superior biological performance.[7,8] While HA supplies abundant Ca^{2+} and PO_4^{3-} ions that serve as nucleation centers for apatite formation-facilitating remineralization and osteointegration, CS confers flexibility and antibacterial effects, promoting uniform HA distribution and improved overall bioactivity.

The mounting clinical demand for bone regeneration/repair materials has underscored the intrinsic weaknesses of HA–CS composite. In particular, its low ductility, poor tensile strength, and inability to form fibers restrict its utility in advanced scaffold fabrication techniques like electrospinning and 3D printing—the current standard for producing porous scaffolds. Consequently, a critical step in advancing bone restoration and regeneration biomaterials is the blending of a high-performance biopolymer, such as poly(ε-caprolactone) (PCL), one possessing superior ductility, tensile strength, and the capability to form fibers/membranes, with HA–CS composite.[9,10]

PCL is a widely used synthetic polymer in bone tissue engineering, valued for its biocompatibility, biodegradability, and favourable mechanical properties. PCL has also been approved by the U.S. Food and Drug Administration for use as an implantable biomaterial, and its relatively low melting temperature (55–60 °C) allows facile processing into scaffolds with diverse architectures. The incorporation of PCL into HA–CS creates a synergistic composite in which the strengths of each component are maximized while their inherent weaknesses are compensated. Specifically, PCL addresses the uncontrollable decomposition of HA–CS, while this composite mitigates PCL's lack of intrinsic biological activity and slow degradation rate under physiological conditions.[11] Recent studies have also reported PCL-based HA/CS composite scaffolds, demonstrating promising *in vivo* osteogenic performance when combined with progenitor or stem cells.[12,13]

Despite these benefits, the use of most synthetic PCL-HA/CS composite scaffolds presents significant trade-offs. Most reported HA–CS in the bioactive composite are synthesized through multi-step processes that require separate sources of calcium and phosphate and/or CS, followed by blending with commercial CS and/or HA.[14–16] As a result, the production costs are often prohibitive. More importantly, the safety and reliability for patients remains questionable, largely due to their synthetic (non-biological) origin and environmentally unsustainable production process.

In another aspect, globally, approximately 8 million tons of crustacean shells,[17] such as crab shells that contain abundant natural calcium carbonate ($CaCO_3$) and chitin – essential components needed for the fabrication of HA–CS composites,[9] are discarded each year—most of which are primarily dumped at sea or sent to landfill.[18] The current disposal practice constitutes a fundamental contradiction: a potentially valuable bioresource is unintentionally transformed into an environmental pollutant and consequently creates substantial environmental hazards and ecological detriment. Although a few initial studies have addressed this challenge, they have only focused on the separate recovery of HA and CS from this abundant resource.[10,19–21] Notably, research on fully deriving HA–CS from crab shells remains scarce, being largely confined to synthesis, with only limited studies exploring its potential applications, and none have addressed its integration into scaffold systems for bone repair and regeneration.[22]

The above analysis underscores a substantial gap in the current research regarding both the synthesis of PCL-based HA/CS composite (utilizing crab shell-derived HA–CS) and its application potential within the field of bone tissue engineering. To bridge this research gap, in this study, we report a novel strategy for the simultaneous synthesis of HA–CS composites directly from crab shells *via* a one-pot process, followed by their incorporation into PCL-based scaffolds for bone regeneration applications. The approach exploits crab shells as a renewable dual precursor for calcium and chitin, enabling a sustainable and cost-effective pathway for bio-composite fabrication while contributing to pollution reduction. The resulting HA–CS composites were thoroughly characterized by XRD, FTIR, SEM, TEM, and TGA to confirm their structural and chemical features. PCL/HA–CS scaffolds with varying blend ratios were subsequently prepared and evaluated for their physicochemical, mechanical, and biological properties, including swelling, degradation, mineralization in simulated body fluid (SBF), cytocompatibility, and antibacterial activity. By bridging sustainability and functionality, this study highlights a scalable biomaterials design strategy that leverages marine biowaste for the development of advanced scaffolds with strong potential in bone tissue engineering.

2 Materials and methods

2.1 Materials

Crab shells were collected from local seafood markets in Da Nang City, Vietnam, thoroughly washed, dried, and ground prior to use. Polycaprolactone (PCL, Mn ~80 000) was purchased from Sigma-Aldrich. Phosphoric acid (H_3PO_4, ≥ 85%), hydrochloric acid (HCl, ~37%), sodium hydroxide (NaOH, ≥ 98%), and other analytical grade reagents were obtained from Xilong Scientific (China) and Fisher Scientific and used without further purification. Phosphate-buffered saline (PBS, pH 7.4) was purchased from Sigma-Aldrich. Simulated body fluid (SBF) was prepared according to the protocol reported by Kokubo and Takadama[23] to mimic the ion concentrations of human blood plasma.

2.2 One-pot synthesis of HA–CS composite

The HA–CS bio-composite was prepared through a simultaneous demineralization, deacetylation, and *in situ* HA precipitation process using crab shells as the raw material. The shells were thoroughly washed with distilled water, dried at 60 °C, ground, and sieved (<0.3 mm). Pigments were removed by soaking the powder in a mixture of 2% H_2O_2 and 50% ethanol (1 : 10, w/v) at 50 °C for 2 h under stirring, followed by drying. The calcium content of the crab shells was preliminarily determined to optimize the stoichiometric ratio of Ca/P for HA synthesis. Briefly, 2 g of the dried and ground crab shell powder was calcined in air at 900 °C for 3 h to completely decompose $CaCO_3$ into CaO. The resulting CaO was dissolved in 1 M HCl

and titrated with standardized EDTA solution to determine the calcium content. The crab shell powder was found to contain approximately 30.96 ± 0.45 wt% Ca. Based on this value, the amount of H_3PO_4 required to achieve a stoichiometric Ca/P ratio of 1.67 for HA formation was calculated.

For the simultaneous synthesis of HA–CS, 2.0 g of the pre-treated crab shell powder was suspended in 20 mL of concentrated HCl (~37%) and stirred for 60 min to achieve demineralization. A stoichiometric amount of H_3PO_4 (85%) was then introduced to supply phosphate ions for HA formation. Subsequently, 100 mL of 5 M NaOH was added, and the mixture was maintained at 105 °C for 60 min under reflux to induce deacetylation of chitin and promote *in situ* precipitation of HA. After cooling to room temperature, the suspension was centrifuged at 8000 rpm and repeatedly washed with distilled water until a neutral pH was reached. The obtained solid was dried at 60 °C to yield the HA–CS composite. The overall synthetic route of the HA/CS composite is schematically illustrated in Fig. 1.

2.3 Characterization of the composite

The structural, morphological, compositional, and thermal properties of the synthesized HA/CS composite were investigated using a range of analytical techniques. The crystalline structure was examined by X-ray diffraction (XRD) using a Shimadzu XRD-6100 diffractometer (Japan) equipped with a Cu-Kα radiation source (λ = 1.5406 Å). The diffraction patterns were recorded in the 2θ range from 10° to 80°, with a step size of 0.02° and a scanning speed of 2° per minute. Fourier-transform infrared spectroscopy (FT-IR) was employed to identify the functional groups present in the composite. The spectra were recorded on a Tensor 27 spectrometer (Bruker, Germany) over the wavenumber range of 4000–400 cm^{-1} using the KBr pellet

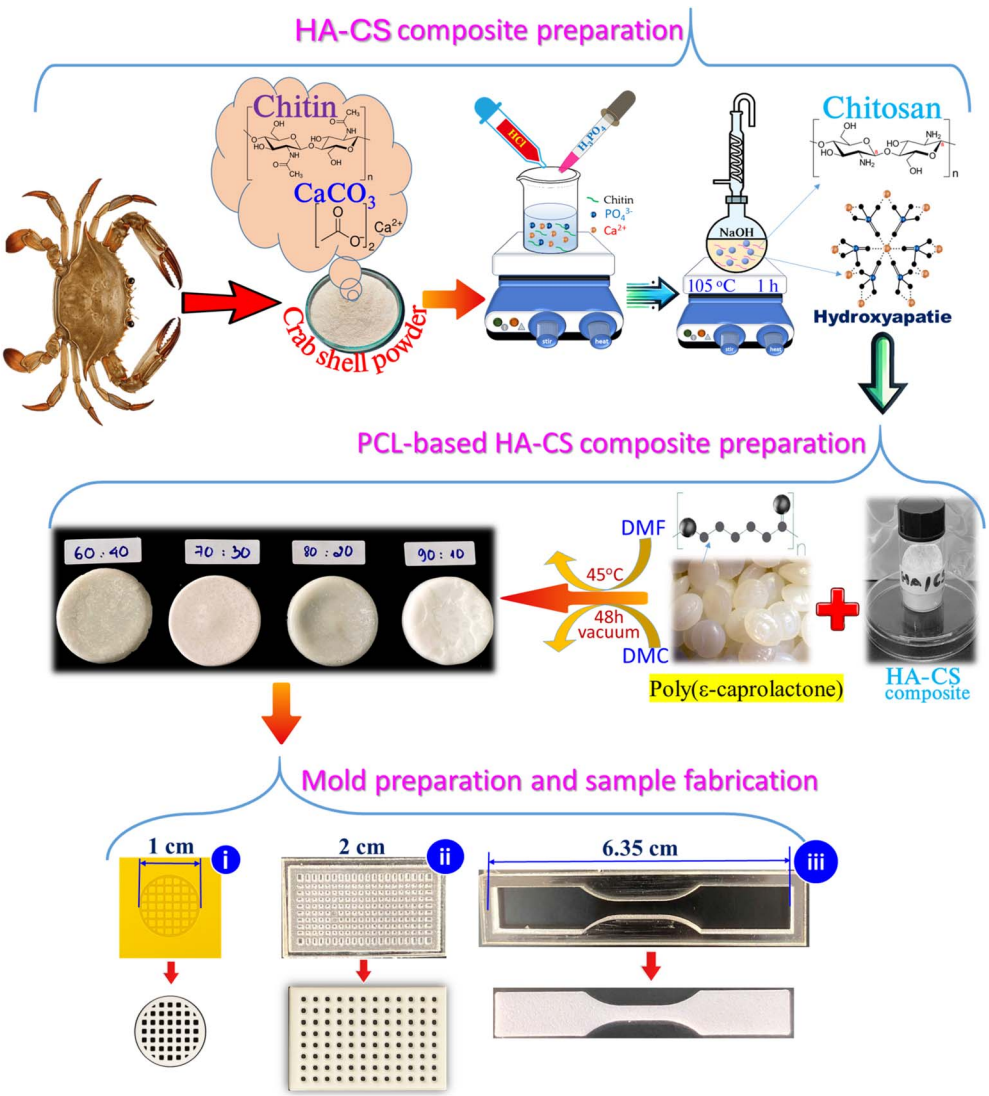

Fig. 1 Schematic illustration of the one-pot synthesis process for HA–CS composite derived from crab shell and PCL/HA–CS composite preparation as well as the fabricated molds and molded composites: (i) circular grid mold (Ø10 mm × 1 mm) and its corresponding specimen; (ii) rectangular grid mold (20 × 15 × 1 mm^3) and specimen; (iii) ASTM D638 Type V "dog-bone" mold and molded tensile specimen.

method. The surface morphology and microstructure of the composite were observed by field emission scanning electron microscopy (FE-SEM, model S-4800) and a conventional scanning electron microscope (Tescan Vega 3, Czech Republic). In addition, the internal nanostructure was analyzed using high-resolution transmission electron microscopy (HR-TEM, JEM 2100, JEOL, Japan). The elemental composition was determined by energy-dispersive X-ray spectroscopy (EDS) attached to the SEM system (Tescan Vega 3). Thermal stability and decomposition behavior were evaluated by thermogravimetric analysis (TGA) using an Evo/LabSys Thermoelectric analyzer (model S60/58988, France). The measurements were conducted under an air atmosphere in the temperature range of 50 to 900 °C, at a heating rate of 10 °C per minute.

2.4 Preparation of PCL-based HA–CS composite

The PCL/HA–CS composites were prepared with five different weight ratios of PCL to the HA–CS mixture. The schematic illustration of PCL/HA–CS preparations and their detailed composition are presented in Fig. 1 and Table 1. Formulations containing less than 60 wt% PCL were not considered, since insufficient polymer content led to poor encapsulation and weak binding of the HA–CS powder, resulting in inhomogeneous mixtures and unstable composites.

In each formulation, 4.0 g of PCL was completely dissolved in 25 mL of a mixed solvent consisting of dichloromethane (DCM, 90%) and dimethylformamide (DMF, 10%) under magnetic stirring at room temperature for 30 min in a fume hood. Subsequently, the corresponding amount of HA–CS powder was gradually added to the polymer solution and stirred for an additional 30 min to ensure uniform dispersion of the filler within the polymer matrix. After mixing, the suspensions were cast into Petri dishes and allowed to evaporate naturally at room temperature inside a fume hood until the majority of the solvent had dissipated. The obtained solid composites were subsequently dried in a vacuum oven at 45 °C under reduced pressure for 48 h to ensure complete removal of the residual high-boiling-point solvent (DMF). The resulting solid composites were rinsed with ethanol to eliminate residual solvent and impurities, followed by drying at room temperature to yield the final PCL/HA–CS.

2.5 Mold preparation and sample fabrication

Custom molds were designed using CAD software (SolidWorks) and fabricated by laser cutting using the Beamo Laser Cutter (Flux Technology, Taiwan) on acrylic plates. Two types of grid molds were prepared: (i) circular molds with 10 mm diameter and 1 mm depth, and (ii) rectangular molds with dimensions of $20 \times 15 \times 1$ mm^3 (Fig. 1). These geometries were selected to facilitate mineralization, water absorption, and degradation tests in PBS solution. For mechanical evaluation, "dog-bone" shaped molds were designed according to ASTM D638 Type V specifications, with dimensions: total length ~63.5 mm, gauge length ~9.53 mm, narrow width ~3.18 mm, and thickness ~3.2 mm.

Prior to casting, the inner surfaces of all molds were lightly coated with a thin layer of vegetable oil to facilitate specimen removal. The required amount of PCL/HA–CS composite was then introduced into the molds and softened by immersion in hot water (70–80 °C) to ensure polymer flow and packing. The softened mixture was subsequently compressed manually to achieve homogeneous compaction, followed by rapid cooling in a refrigerator (~10 min) to solidify the specimens. The molded composites were carefully demolded and stored in a desiccator until further use.

Table 1 Compositions of PCL/HA–CS composites with different PCL-to-HA–CS weight ratios

Sample	PCL/HA–CS (wt%)	PCL (g)	HA–CS (g)
M1	100 : 0	4.0000	0.0000
M2	90 : 10	4.0000	0.4444
M3	80 : 20	4.0000	1.0000
M4	70 : 30	4.0000	1.7143
M5	60 : 40	4.0000	2.6667

2.6 Biological and mechanical evaluation

2.6.1 Antibacterial activity assessment. The antibacterial activity of the prepared scaffolds was evaluated initially using the disc diffusion method to assess their inhibitory effects against representative pathogenic bacteria. Two strains were selected: *Staphylococcus aureus* (Gram-positive) and *Escherichia coli* (Gram-negative). Bacterial suspensions were cultured in nutrient broth at 37 °C for 24 h, reaching the logarithmic growth phase, and then diluted to approximately 10^6 colony-forming units per milliliter (CFU mL^{-1}). A uniform bacterial lawn was prepared by spreading 100 μL of the suspension onto Mueller–Hinton agar (MHA) plates. The test specimens, including pure HA, HA–CS composite, and the PCL/HA–CS (80 : 20) blend, were fabricated into discs of ≈ 6 mm in diameter and sterilized by UV irradiation (254 nm, 30 min each side). Ampicillin (10 μg per disc) was used as a positive control, while a sterile blank disc without material served as the negative control. The plates were then incubated at 37 °C for 24 h. Antibacterial efficacy was quantified by measuring the diameter of the clear inhibition zone surrounding each sample. The final zone of inhibition was reported by subtracting the sample diameter from the total measured clear zone diameter.

The minimum inhibitory concentration (MIC) and minimum bactericidal concentration (MBC) of the HA, HA–CS, and PCL/HA–CS (80 : 20) scaffolds were also determined against *S. aureus* and *E. coli* using the broth microdilution method. Stock dispersions of each sample were prepared in 10% DMSO and serially diluted in Mueller–Hinton broth (MHB) to obtain final concentrations ranging from 0.08 to 10 mg mL^{-1}. Bacterial suspensions were adjusted to approximately 10^6 CFU mL^{-1}, and 100 μL of each bacterial inoculum was added to an equal volume of the sample solution in 96-well microplates (total volume 200 μL per well). Wells containing 10% DMSO in MHB served as the negative control, while ampicillin (10 μg mL^{-1}) was used as the positive control. After incubation at 37 °C for 24 h, 20 μL of 0.01% resazurin solution was added to each well,

followed by an additional 2 h incubation. A color change from blue to pink indicated bacterial growth, whereas an unchanged blue color indicated inhibition. The MIC value was defined as the lowest concentration of the sample that prevented the color change of resazurin compared with the controls. To determine the MBC, all aliquots from wells showing no color change (no visible growth) were spread onto Tryptic Soy Agar (TSA) plates and incubated at 37 °C for 24 h. The MBC was defined as the lowest concentration at which it corresponds to ≥ 99.9% killing of the initial inoculum.

2.6.2 Cytotoxicity test. Cytotoxicity was assessed using human foreskin fibroblasts (HFF-1; ATCC® SCRC-1041™, USA) following the protocol recommended by the U.S. National Cancer Institute (NCI), with sulforhodamine B (SRB) assay as the readout. HA, HA–CS, and PCL/HA–CS (80 : 20) were dissolved in DMSO to prepare stock solutions (100 μg mL^{-1}), then diluted in serum-free medium. Cells were seeded in 96-well plates and incubated for 18–20 h at 37 °C in a CO_2 incubator prior to sample treatment. After 48 h exposure, cells were fixed with trichloroacetic acid (TCA), stained with SRB, washed with 1% acetic acid, and absorbance was recorded at 540 nm. Experiments were performed in triplicate. Ellipticine (0.08–10 μg mL^{-1}) was used as the positive control, while 1% DMSO served as the negative control. IC_{50} values were determined using TableCurve 2Dv4 software.

2.6.3 Assessment of composite hydrophilicity. Hydrophilicity of the composites was characterized *via* water uptake and contact angle measurements. In particular, the water absorption capacity of the scaffolds was evaluated by immersing pre-weighed dried samples (W_0) in phosphate-buffered saline (PBS, pH 7.4) at 37 °C. At predetermined time intervals, the samples were removed, gently blotted to eliminate surface moisture, and immediately weighed (W_t). The adsorption ratio was calculated using the mathematical equation (eqn (1)):

$$\text{Water uptake}(\%) = \frac{W_t - W_0}{W_0} \times 100 \quad (1)$$

where W_0 is the initial dry weight, and W_t is the weight at time *t*.

Water contact angles were measured by the sessile drop method using a DataPhysics OCA analyzer, employing a 2 μL droplet of deionized water.

2.6.4 Biodegradation in simulated physiological conditions. The biodegradability of the scaffolds was investigated by monitoring weight loss in PBS (pH 7.4) at 37 °C over different incubation periods. Pre-weighed dried samples (m_0) were immersed in 10 mL of PBS and kept under static conditions. At scheduled time intervals, the samples were collected, rinsed with distilled water, dried at 60 °C until constant weight, and re-weighed (m_t). The percentage of weight loss was determined using the mathematical equation (eqn (2)):

$$\text{Weight loss}(\%) = \frac{m_0 - m_t}{m_0} \times 100 \quad (2)$$

All tests were conducted in triplicate ($n = 3$), and data were reported as mean ± SD.

2.6.5 Mechanical properties. Tensile strength of the scaffolds was measured using a universal testing machine (Shimadzu AG-X, Japan) in accordance with ASTM D638. Dog-bone-shaped samples (Type V) were tested at a crosshead speed of 5 mm min^{-1}. The maximum force, ultimate tensile strength (UTS), and Young's modulus were determined from the stress–strain curves. Although elongation at break was also recorded from crosshead displacement, these values may overestimate the true strain due to system compliance and were therefore not included in the analysis.

2.6.6 *In vitro* mineralization in SBF. The bioactivity of the scaffolds was evaluated by soaking them in simulated body fluid (SBF, pH 7.4) at 37 °C for 14 days. After immersion, the samples were rinsed with deionized water, dried, and analyzed using SEM and EDX to observe apatite layer formation on the scaffold surfaces.

3 Results and discussion

3.1 Characterization and formation mechanism of HA–CS composite from crab shell

Crab shell is an abundant biowaste rich in $CaCO_3$ and chitin—two key precursors for the simultaneous synthesis of HA and CS. In this study, the HA–CS composite was directly synthesized from crab shell through a simple yet effective chemical process that integrates two parallel pathways: the precipitation of HA from the inorganic component ($CaCO_3$), and the deacetylation of chitin to form CS from the organic matrix of the shell. Upon completion of the goal-directed composite synthesis, the FTIR spectroscopy was subsequently performed to confirm the chemical transformation from the chitin/$CaCO_3$ precursor to the final HA–CS composite, specifically verifying the deacetylation of chitin into CS and the formation of characteristic HA functional groups. Composed primarily of $CaCO_3$ (50–70% wt) and chitin (30–40%), the FTIR spectrum of the raw crab shell powder (red line) displays enhanced contribution of these compounds (Fig. 2a). The prominent absorption bands observed at 1415, 875, and 713 cm^{-1} are characteristic of the calcite crystalline phase of mineralized calcium carbonate. Furthermore, the broad band in the region of ~3480–3740 cm^{-1}, together with strong vibration at 1655 cm^{-1}, and doublet at 1070 and 1030, are assigned to the stretching vibrations of O–H and N–H groups, ν(C=O) of amide (I) and ν(C–O) of polysaccharide backbone vibrations of chitin, respectively. Needless to say that following mineralization and *in situ* precipitation, the vibrational spectra of the obtained composite display pronounced spectral variations, indicating substantial structural and compositional changes. The $CaCO_3$ signal was no longer observable, and new absorption bands appeared in the ranges of 1030–1080 cm^{-1}, 600–630 cm^{-1}, and around 895 cm^{-1}, which are characteristic of the asymmetric (ν_3, ν_4) and symmetric (ν_1) P–O stretching modes of PO_4^{3-} vibrations in HA, respectively.[24,25] Notably, the disappearance of the amide (I) band – the most prominent peak of chitin, and the simultaneous emergence of N–H deformation of amide (II) at 1525 cm^{-1}, assigned to CS, initially confirms successful deacetylation of chitin and the material transformation.[26]

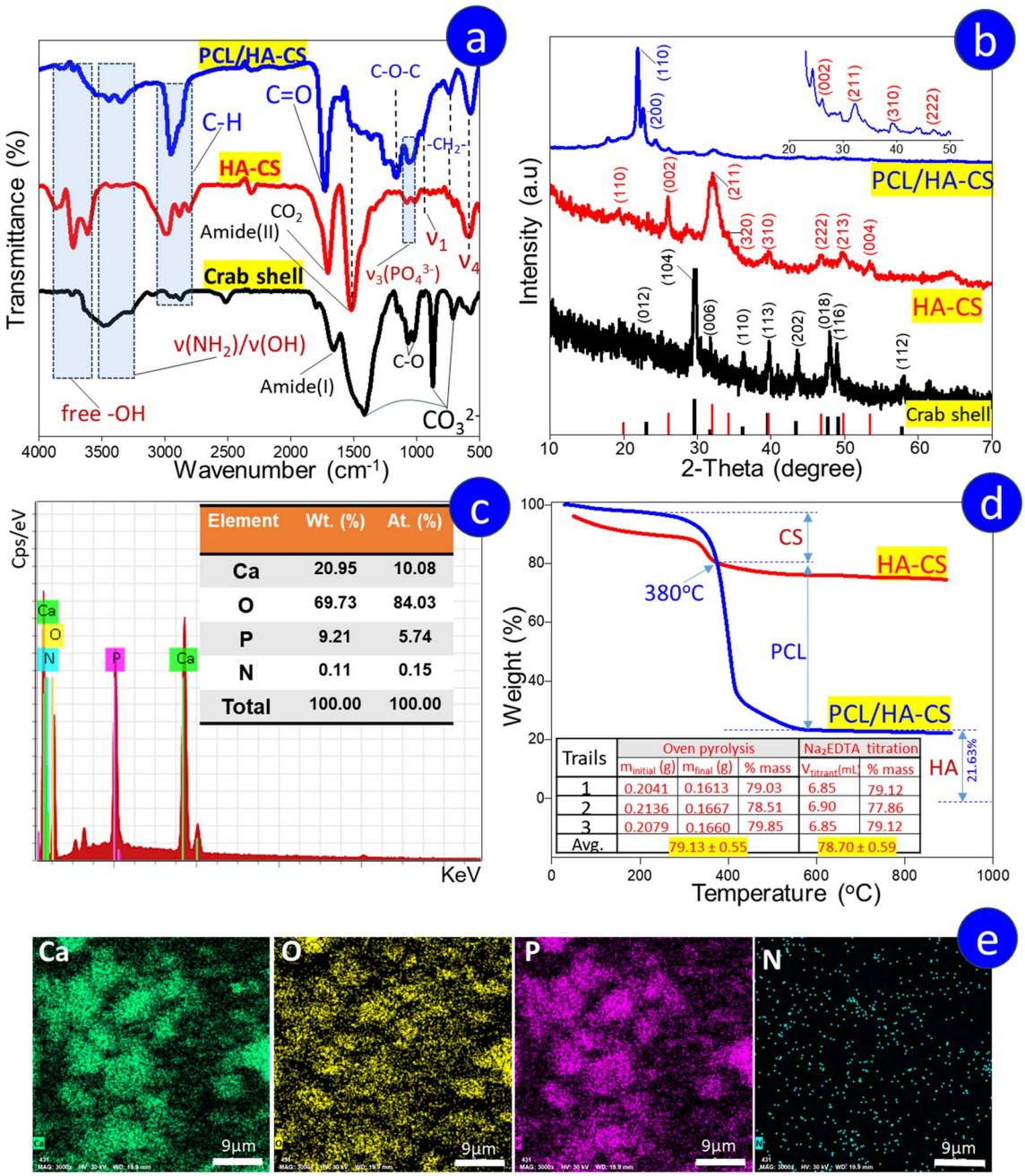

Fig. 2 FT-IR spectra of crab shell powder and its derived materials (a); their corresponding XRD patterns (b); elemental composition of HA–CS (c); TGA diagrams of HA–CS and PCL/HA–CS (d), as well as elemental distribution map of HA–CS (e).

Additionally, the characteristic band of the $-NH_2$ group at around 1335 cm^{-1} became more intense after the *N*-deacetylation of chitin, confirming the presence of CS in the targeted HA–CS composite. Interestingly, the C–H and CH_2 bands of the polysaccharide framework became more pronounced in the FT-IR spectrum of HA–CS composite. This observation is consistent with results reported following the synthesis of CS from chitin.[27] This spectral enhancement suggests that deacetylation—which removes the $-COCH_3$ group and forms $-NH_2$ – reduces crystalline order and increases polymer flexibility. This, in turn, may release constrained modes, thereby clarifying and intensifying the C–H stretching signal. At the same time, the band around 3400–3700 cm^{-1} persists, with increased intensity and slight shifts, reflecting the continued presence of $-NH_2$ and free hydroxyl –OH functional groups in CS, respectively.[28] It should be noted that the –OH and –NH functional groups of pure CS are typically engaged in hydrogen bonding interactions, which are generally manifested as broad vibrational bands within the range of 3200–3500 cm^{-1} of FT-IR spectrum.[29] However, the emergence of sharp, distinct signals between 3500–3700 cm^{-1} characteristic of free –OH groups was exclusively observed in the spectra of CS composites,[30–33] including the current case.

The observed spectral shift, characterized by the enhancement of the narrow vibration indicative of free OH groups concurrent with a significant reduction in the broad hydrogen-bonded OH band, provides strong spectroscopic evidence for a decrease in intramolecular hydrogen bonding.[34] This phenomenon typically accompanies the successful bonding of OH-containing polymers to a second compound, where the structural constraint or chemical environment favours the disruption of internal hydrogen networks.[35] Additional evidence from the FT-IR analysis supports this interpretation. The distinguishing absorption peak for the amide (II) moiety in CS typically appears at 1550–1560 cm^{-1}.[36,37] However, upon linkage to another component such as inorganic through the –NH functional group, this band is significantly shifted to a lower wavenumber.[38,39] The observation of the peak at 1525 cm^{-1} in our analysis directly supports the presence of this interaction in HA–CS composite. These findings strongly suggest that HA interacts with SC through the NH group, resulting in the formation of HA–CS composite.

More interestingly, upon mixing HA–CS with the PCL matrix, which contains a dense C=O and C–O network, the vibrational bands of the free OH group disappear, while the broad OH stretching band associated with hydrogen bonding re-emerges. This spectral change is consistent with the formation of hydrogen bonds between OH groups and the C–O/C=O network. In addition to the OH/NH stretching vibrations, the FT-IR spectrum of PCL/HA–CS shows several distinctive features. Accordingly, strong absorptions at 2966 cm^{-1} – 735 cm^{-1}, and 1735 cm^{-1} correspond to CH_2 stretching vibration within the polymer backbone and the signature C=O stretching band of PCL, respectively, while the band near 1160 cm^{-1} arises from C–O–C asymmetric stretching. Moreover, the retention of diagnostic bands assigned to AH and CS in the spectrum of the targeted composite supports the successful incorporation of PCL with HA–CS.

The XRD results further confirmed the conclusions drawn from the FT-IR analysis. Fig. 4a shows the XRD patterns of two samples: (1) pretreated crab shell powder (red line), and (2) the synthesized HA–CS composite (blue line) (Fig. 2b). Consider first the XRD pattern of PCL-based HA/CS composite, which displays a distinct diffraction peak at $2\theta \approx 21.89°$ (110), indexed to the orthorhombic crystalline phase of PCL. In addition to the reflection centered near $2\theta \approx 21.89°$, pure PCL is also characterized by a signal at $2\theta \approx 23.8°$, which is indexed to the (200) plane. The emergence of a new diffraction peak at $2\theta = 22.65°$ in the PCL–HA/CS pattern can be shifted from the characteristic peak at $2\theta \approx 23.8°$, likely induced by the incorporation of PCL within the composite matrix.[40] Notably, the characteristic diffraction peaks of CS and HA in the HA–CS composite become very weak but remain detectable in the XRD pattern of PCL–HA/CS, suggesting that these components are embedded within the PCL matrix, which may hinder their crystallographic reflections. Those reflections can be indexed to the planes (002), (211), (202), (310), (222), and (213) at approximately $2\theta = 26°$, 31.7°,34.1°, 39.8°, 46.7° and 49.5°, respectively, which are in good agreement with the standard JCPDS card No. 00-009-0432 corresponding to the hexagonal HA structure. Additionally, a broad diffuse background (elevated baseline) in the low-angle region (8°–10°) and a sharp peak at $2\theta = 19.2°$ (110) are observed in HA–CS pattern, which is indicative of the presence of an amorphous CS phase. These findings further support the successful conversion of crab shells into HA–CS composite during the synthesis process. Parallelly, the XRD results agreed well with the FT-IR findings, indicating that $CaCO_3$ in the raw shells crystallizes in the calcite phase. The observed reflection at $2\theta \approx 23.2°$ (012), 29.4° (104), 31.7° (006), 36.1° (110), 39.5° (113), 43.1° (202), 47.8° (018), 48.9° (116), and 57.4° (112) matched well with the calcite JCPDS card no. 86-2340.[41,42] As expected, these diffraction peaks disappeared completely upon transformation of crab shells into HA–CS composite. Overall, these results confirm that crab shell can be effectively utilized as a dual source of calcium and chitin for the simultaneous formation of HA and CS, and that the one-pot synthesis strategy successfully produced an HA–CS composite with a well-defined HA phase.

To further substantiate this conclusion and gain deeper insights into the HA composition – a key component in bone regeneration, additional quantitative analyses, including EDS, TGA, thermal decomposition analysis, and complexometric titration using Na_2EDTA, were performed.

The EDS spectrum obtained from the selected region of HA–CS composite (Fig. 2c) clearly displays the characteristic peaks of the major elements present in the sample. Calcium (Ca) and phosphorus (P) are the main constituents of HA, with oxygen (O) arising from phosphate (PO_4^{3-}) and hydroxyl (OH^-) groups. The presence of nitrogen (N) is attributed to the amine groups (–NH_2) in CS, which form *via* deacetylation of chitin during the synthesis process. Quantitative analysis using the EDX analysis software (table embedded in Fig. 2c) revealed that Ca and P accounted for 20.95% and 9.21%, respectively, yielding a Ca/P molar ratio close to the theoretical value of 1.67 for stoichiometric HA. The elemental mapping images (Fig. 2e), illustrating the spatial distribution of individual elements across the HA–CS composite, indicate that Ca, O, and P are uniformly distributed, suggesting homogeneous dispersion of HA throughout the material. Nitrogen signals are also observed at multiple locations, providing further evidence of the incorporation of CS into the composite matrix. These results further confirm the successful chemical integration of HA and CS within the synthesized material and provide strong support for the efficient conversion of crab shell components into a functional HA–CS composite.

The TGA curves (Fig. 2d) of HA–CS and PCL/HA–CS composites exhibit two distinct stages of mass loss associated with pyrolysis. The first stage, occurring below 150 °C, corresponds to the typical desorption of surface and bound water molecules, whereas the second stage (200–420 °C for HA–CS and 200–600 °C for PCL/HA–CS, with major peaks at 360 °C and 400 °C, respectively) is attributed to the thermal decomposition of organic component.[43] Particularly, below 200 °C, the mass loss of HA–CS reached approximately 10%, whereas that of PCL–HA/CS composite was only 3.1%. This observation suggests that the PCL component in the biological composite possesses intrinsic hydrophobicity. For the second stage, the TGA curves of HA–CS and PCL–HA/CS intersect near 380 °C,

coinciding with the main decomposition peak and inflection point of HA–CS. This temperature also corresponds to the onset of weight loss in PCL–HA/CS,[44] indicating a two-step degradation pathway: below 380 °C, the thermal behavior resembles that of CS, whereas above 380 °C, it reflects the intrinsic decomposition of PCL. At temperatures above 800 °C, all samples reached a stable plateau, indicating the thermally stable inorganic residues, corresponding to HA. These two stages accurately reflect the decomposition behaviors of inorganic and organic compounds within the studied composite. Furthermore, these two events account for a total mass loss of 21.63%, leaving 78.37% of the HA–CS intact at 800 °C. This residual mass is primarily attributed to the thermally stable inorganic phase (HA). This finding agrees with the residual inorganic content after pyrolysis of PCL/HA–CS (the TGA sample containing 30% HA–CS) which remains at about 22.52% at the same temperature. The relatively high residual mass confirms the formation of a HA-rich composite, consistent with the intended synthesis approach using crab shell as a dual precursor for calcium and chitin. However, to improve reliability, the HA content was further validated through an independent method—complexometric titration and the 800 °C/90 min oven pyrolysis of HA–CS composite. Complexometric titration using disodium ethylenediaminetetraacetate (Na_2-EDTA) is a classical but highly accurate method for quantifying calcium ions (Ca^{2+}) in materials. Since calcium in the composite originates mainly from HA, the Ca^{2+} concentration can be used to indirectly determine the HA content. The procedure involves dissolving the HA–CS sample in HCl, followed by complexation with Na_2EDTA and back-titration using a standard $MgSO_4$ solution with Eriochrome Black T as the indicator.[45] The percentage of HA was calculated based on the stoichiometric relationship in HA, which contains 10 moles of Ca^{2+} per mole of HA. Triplicate measurements were performed to ensure reproducibility. Each of the two additional analyses was conducted in triplicate to verify reproducibility. The average HA content obtained from titration and pyrolysis (table within Fig. 2d) was 78.70% ± 0.59% and 79.13 ± 0.55, respectively, which is in excellent agreement with the 78.37% value determined by TGA. These results confirm both the compositional integrity and the effectiveness of the one-pot synthesis strategy in producing a HA-rich composite material from crab shell waste.

To investigate the surface morphology and microstructure of the synthesized HA–CS composite, SEM and TEM techniques were employed. Fig. 3 presents SEM images (a and b) and TEM images (c and d) of the HA–CS composite at various magnifications. Fig. 3a shows an SEM image taken at a magnification of 300 00×, revealing a porous surface structure with numerous agglomerated particles tightly bonded together. This is a typical morphological feature observed in HA/CS composites and is consistent with previous findings reported by Hsu *et al.*[24] At higher magnification (800 00×), as shown in Fig. 3b, individual crystalline particles can be more clearly distinguished, embedded within the polymer matrix. These particles exhibit short rod-like or flake-like morphologies, characteristic of HA nanocrystals.

TEM imaging further confirmed the nanoscale structure of the composite. Fig. 3c, captured at approximately 1 000 00× magnification, reveals plate-like and rod-like HA crystals with sizes ranging from 20 to 100 nm. These observations confirm the successful formation of nanoscale HA, which is considered ideal for applications in bone tissue scaffolds due to its high surface area and bioactivity. In the high-resolution TEM image shown in Fig. 3d (~5 000 00× magnification), a faint

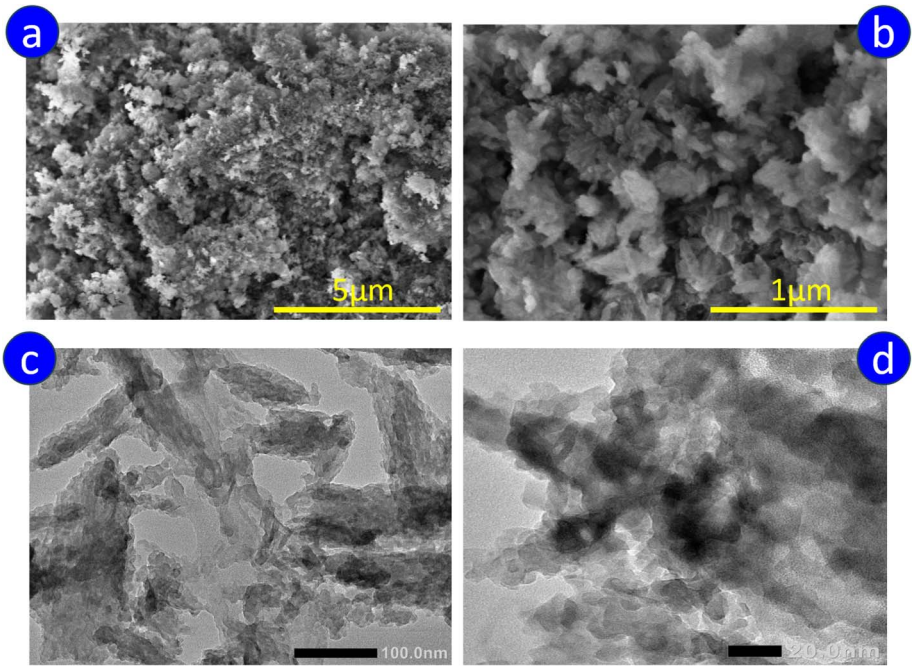

Fig. 3 SEM (a and b) and TEM (c and d) images of HA–CS composite at varying resolutions.

amorphous matrix can be observed surrounding the crystalline HA nanoparticles. Because CS is inherently a semi-crystalline polymer[46] with intrinsically low electron density, its phase typically exhibits weak contrast and is therefore difficult to resolve under TEM.[47] The faint diffuse matrix observed in the micrographs is thus most plausibly attributed to CS domains encapsulating the HA particles, indicating good dispersion and integration between the two components. Overall, the SEM and TEM analyses confirm that the synthesized composite possesses a nanoscale microstructure, with well-dispersed HA nanocrystals embedded within the CS matrix. Such morphology is favorable for enhancing biocompatibility and promoting cell adhesion and proliferation, which are essential properties for bone tissue engineering applications.

Based on the material characterization analyses, the implemented synthesis procedure was confirmed to be effective for the preparation of PCL/HA–CS derived from crab shell. It should be noted that HA synthesized from natural calcium sources, particularly under simultaneous demineralization and *in situ* precipitation conditions, is unlikely to be fully stoichiometric. For the sake of clarity and simplicity, the reaction equations presented in this study assume the formation of stoichiometric HA; however, the actual product may contain non-stoichiometric features typical of naturally derived HA. The formation mechanism of PCL/HA–CS is proposed as follows: after demineralization with HCl (eqn (3)) and phosphorus supplementation using H_3PO_4, the crab shell powder underwent an alkalization step that simultaneously induced HA precipitation (eqn (4)) and chitin deacetylation (eqn (5)) reactions, yielding substances HA and CS, respectively. Subsequently, resultant HA reacted with CS through NH_2 groups to form the intermediate HA–CS composite (eqn (6)). When blended with PCL, the dangling hydroxyl groups (–OH) in HA–CS further reacted to produce the final composite PCL/HA–CS (eqn (7)). From an initial input of 2.0 g of crab shell powder, the dry yield of HA–CS composite was 1.15 ± 0.07 g, corresponding to a synthesis efficiency of 57.33% ± 3.47%. This represents a relatively high yield for a simultaneous dual-phase synthesis process using unrefined biological feedstock. Additionally, the process occurred in a single reaction system, requiring minimal equipment and fewer purification steps, demonstrating the efficiency and practicality of this one-pot approach for converting natural biowaste into functional biomaterials.

$$CaCO_3 + 2HCl \rightarrow Ca^{2+} + CO_2\uparrow + H_2O + 2Cl^- \quad (3)$$

$$10Ca^{2+} + 6PO_4^{3-} + 2OH^- \rightarrow Ca_{10}(PO_4)_6(OH)_2\downarrow \quad (4)$$

$$(C_8H_{13}NO_5)_n + n\mathrm{NaOH} \rightarrow (HO\text{–}C_6H_8O_3\text{–}NH_2)_n + n\mathrm{CH_3ONa} + n\mathrm{H_2O} \quad (5)$$

$$HO\text{–}C_6H_8O_3\text{–}NH_2 + Ca_{10}(PO_4)_6(OH)_2 \rightarrow HO\text{–}C_6H_8O_3\text{–}NH_2\cdots Ca_{10}(PO_4)_6(OH)_2 \quad (6)$$

$$HO\text{–}C_6H_8O_3\text{–}NH_2\cdots Ca_{10}(PO_4)_6(OH)_2 + (C_5H_{10}\text{–}COO)_n \rightarrow (C_5H_{10}\text{–}COO)_n\cdots HO\text{–}C_6H_8O_3\text{–}NH_2\cdots Ca_{10}(PO_4)_6(OH)_2 \quad (7)$$

3.2 Water uptake and biodegradation behavior of PCL/HA–CS scaffolds in simulated physiological conditions

The interaction of scaffolds with aqueous environments is a pivotal factor influencing their performance in bone tissue engineering, affecting cell attachment, nutrient diffusion, and degradation kinetics. In this study, the water uptake, water contact angles and biodegradation behavior of PCL/HA–CS plate-like scaffolds (20 × 15 × 1 mm^3) were evaluated under simulated physiological conditions (PBS, 37 °C) to assess their suitability for bone defect repair, and the results are shown in Fig. 4. The water absorption results (Fig. 4a) revealed a progressive increase in swelling with the incorporation of HA–CS. The pure PCL scaffold (M1) exhibited the lowest uptake (~1.5%), consistent with its hydrophobic and semi-crystalline nature. By contrast, composites containing HA–CS showed higher water absorption, with M5 (40 wt% HA–CS) reaching the maximum (~11%). This observation was further validated through contact angle measurements (Fig. 4b), which were conducted to assess the surface hydrophilicity of the composites. Accordingly, pristine PCL, which is inherently hydrophobic, exhibited a high contact angle of approximately 102°. In contrast, the PCL–HA/CS composites showed contact angles below 90°—a characteristic of hydrophilic surfaces[48] —with the obtained values progressively decreasing as the mineral content increased (from about 88° down to 64°). This trend can be attributed to the intrinsic hydrophilicity and water adsorption-favourable architecture of the HA–CS composite. Specifically, the HA phase, which constitutes the major component, possesses abundant water-adsorption sites (Ca^{2+} and OH^-) and contributes significantly to the surface roughness of the composite and interconnected micro-porosity, thereby promoting liquid penetration. As observed in the SEM images (Fig. 3a and b), the composite exhibits a rough and porous morphology that facilitates water uptake. Although CS is incorporated in a relatively small proportion and thus plays a secondary role, its amino and hydroxyl groups may contribute modestly through hydrogen bonding interactions with water, thereby also improving scaffold hydrophilicity.[49] The increase in water uptake with higher HA–CS content therefore reflects both compositional hydrophilicity and microstructural modifications of the composite scaffolds. Generally, enhanced hydrophilicity is instrumental in promoting protein adsorption, which subsequently facilitates cell adhesion, proliferation, and differentiation.[50] Notably, the water uptake capacity of PCL/HA–CS increases linearly with the amount of CS and HA incorporated, following the relation $y = 0.2488[\text{HA–CS}] + 1.382$, $R^2 = 0.9997$. This proves that hydrophilic sites are uniformly dispersed within the PCL matrix, without noticeable agglomeration.[49]

The biodegradation profile (Fig. 4c) revealed a clear time-dependent mass loss over 8 weeks. Pure PCL (M1) showed negligible degradation (<1.5% at week 8), reflecting its slow hydrolytic breakdown. By contrast, scaffolds containing HA–CS exhibited significantly higher degradation rates, which increased with higher CS content. After 8 weeks, M2 (90 : 10) lost ~6.6% of its mass, M3 (80 : 20) lost ~11.3%, M4 (70 : 30) lost

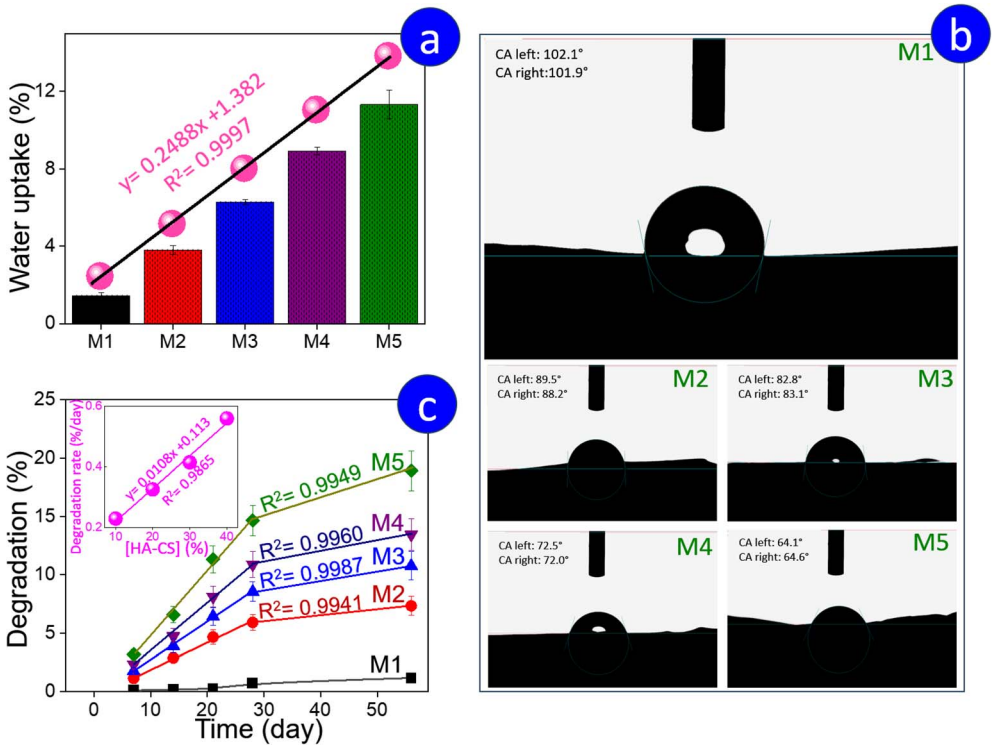

Fig. 4 Water uptake capacity of the HA–CS/PCL scaffolds after 24 h immersion in PBS solution (pH 7.4 at 37 °C) (a) and their water contact angles (b); *in vitro* degradation kinetics (mass loss percentage) of the HA–CS/PCL scaffolds over 8 weeks in PBS solution (pH 7.4 at 37 °C) (c).

~14.7%, and M5 (60 : 40) exhibited the most pronounced mass loss of ~18.9%. Statistical analysis confirmed significant differences between groups at each time point ($p < 0.05$). The enhanced degradation is attributable to two main effects: (i) the hydrophilic and enzymatically labile nature of CS, which promotes water penetration and accelerates polymer chain scission; and (ii) the ionic exchange properties of HA, which may induce localized pH fluctuations and further contribute to matrix erosion. These findings are consistent with previous reports emphasizing the interplay between scaffold composition, hydrophilicity, and degradation kinetics. For instance, Abdian *et al.*[51] studied CS/HA scaffolds incorporating mesoporous SiO_2–HA particles and reported significantly higher water absorption (28–43%) compared to our values (<12%). This discrepancy is largely attributable to differences in scaffold architecture: their mesoporous, sponge-like scaffolds provided large pore volumes and rapid water infiltration, whereas the present study employed dense, cast plate-like scaffolds, which inherently limited fluid uptake due to their compact architecture and reduced accessible pore volume. Unlike 3D-printed or foamed scaffolds with high porosity (60–90%), the cast scaffolds exhibited reduced porosity, restricting water penetration and limiting the relative percentage change upon hydration.[52] Similarly, Abdian *et al.*[51] observed reduced degradation in HA- or SiO_2-containing scaffolds relative to pure CS, underscoring the complex role of inorganic fillers in modulating scaffold stability. In contrast, our results showed that HA–CS addition accelerated mass loss relative to pure PCL, but the overall extent of degradation remained substantially lower than that of highly porous CS-based scaffolds.

Notably, the kinetic analysis of PCL/HA–CS biodegradation reveals that during the first four weeks, the mass loss rate increases linearly with time. Moreover, the slope of this linear increase rises proportionally with the HA–CS composition, following the relation $\nu = 0.0108\,[\text{HA–CS}] + 0.1133$ ($R^2 = 0.9865$), where ν is the biodegradation rate (% weight loss per day). This trend has two implications. First, strong linearity supports the water uptake analysis, indicating that HA–CS is uniformly distributed within the matrix, without agglomeration or any threshold/saturation effects. Second, the biodegradation of PCL/HA–CS-based scaffold can be controlled by adjusting the HA–CS component, particularly at least within the first four weeks after implantation — a critical period corresponding to angiogenesis and woven bone formation.[53] This is a critical period that demands precise control of degradation, since rapid loss compromises structural integrity, while slow degradation limits cellular infiltration and mineral deposition.

Following the initial period, the mass loss rate decreased sharply. This observation is consistent with the presence of a residual structure enriched in highly crystalline PCL and/or HA-rich phases that are resistant to hydrolysis, which subsequently leads to a diffusion-limited degradation state. The observed kinetics imply that the scaffold architecture is optimized to ensure mechanical robustness at the onset and sustained integrity during the initial phase of bone formation.

The combined results highlight a balance between water uptake and long-term stability. On one hand, the inclusion of

HA–CS improved scaffold hydrophilicity, thereby supporting fluid penetration and potentially enhancing cell attachment and proliferation. On the other hand, the low degradation rate indicates that the scaffolds can preserve their dimensional integrity and mechanical support for extended periods. This property is advantageous for bone defect repair, where scaffolds are required to maintain structural stability during the initial phases of new bone formation. While rapid degradation could be beneficial for complete scaffold replacement by native tissue, excessive loss of mechanical integrity at early stages is undesirable.[54] In this regard, the present PCL/HA–CS composites provide a controlled degradation profile, ensuring stability while offering hydrophilic sites that promote biological interactions. Future optimization may involve blending with faster-degrading polymers (*e.g.*, PLA, PGA) or tuning the HA–CS ratio to tailor the resorption rate to specific clinical needs.

3.3 Mechanical properties

The mechanical strength of bone scaffolds plays a critical role in maintaining their structural integrity during implantation and subsequent tissue regeneration. In this study, tensile testing was conducted on dog-bone-shaped PCL/HA–CS composites prepared according to ASTM D638 Type V. Representative stress–strain curves for the five PCL/HA–CS composite scaffolds (M1–M5) are shown in Fig. 5a, and the corresponding bar chart of Young's modulus and ultimate tensile strength (UTS) is given in Fig. 5b.

As shown in Fig. 5a, all specimens exhibit a typical polymeric composite tensile response: an initial linear elastic region, a yielding/strain-hardening regime, followed by failure. Among the formulations, M1 (100% PCL) exhibited the highest ultimate tensile strength (UTS = 28.6 MPa) and stiffness (Young's modulus, E = 27.7 MPa), reflecting a balance of strength and elasticity. In contrast, formulations M2 and M3 with moderate HA–CS filler (10–20 wt%) demonstrate lower stiffness (E = 8.3 and 7.9 MPa, respectively) but maintain high UTS (~18–19 MPa), reflecting a more ductile behavior. Interestingly, M4 and M5—containing higher filler loadings (30–40 wt%)—show markedly increased stiffness (E = 45.9 and 50.5 MPa, respectively) yet much lower UTS (15.0 and 11.9 MPa), indicating a transition toward brittle behavior with increasing inorganic content.

The observed trend can be rationalised as follows: at low to moderate HA–CS content (10–20 wt%), the inorganic particles act as stress-redistributors and toughening agents within the PCL matrix, promoting load transfer without overly restricting chain mobility. However, at higher loadings (≥30 wt%), the filler network becomes dominant, resulting in constrained polymer mobility, increased interfacial stresses, and particle agglomeration, which elevate stiffness but reduce the scaffold's ability to plastically deform before fracture. This non-linear trend reflects a trade-off: moderate filler enhances load transfer without severely restricting polymer chain mobility, while excessive filler causes particle agglomeration and stress concentration, reducing strength. A similar observation was reported by Lu *et al.*, where injection-moulded PCL/HA dog-bones showed increasing modulus and UTS up to 20 wt% HA, attributed to effective PCL–HA interactions. In contrast, our cast composites demonstrate that beyond ~30 wt% filler, the loss of ductility outweighs reinforcement.[55] Farasati Far *et al.* further showed that in CS/collagen/PCL films, higher PCL fractions consistently improved both tensile strength and elongation, consistent with the ductile nature of PCL.[56] Among the composites, M4 (70 : 30) shows mechanical properties closest to trabecular bone, while M3 (80 : 20) provides a better compromise between mechanical performance and ductility. Depending on the clinical requirement (load-bearing *vs.* flexibility), either formulation could be considered optimal.

3.4 *In vitro* evaluation of antibacterial activity and cytotoxicity

One of the critical requirements for implantable scaffolds in bone tissue engineering is their ability to resist bacterial colonization, thereby reducing the risk of post-surgical infections. In this study, the antibacterial properties of HA, HA–CS, and PCL/HA–CS composites were assessed against representative

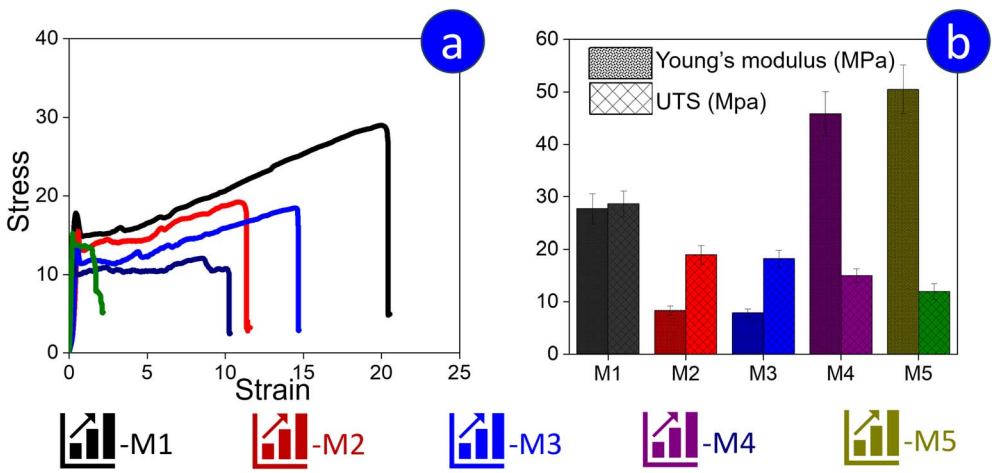

Fig. 5 Engineering stress–strain curves for PCL/HA–CS composites (M1–M5) (a); and bar charts comparing Young's modulus and UTS (b).

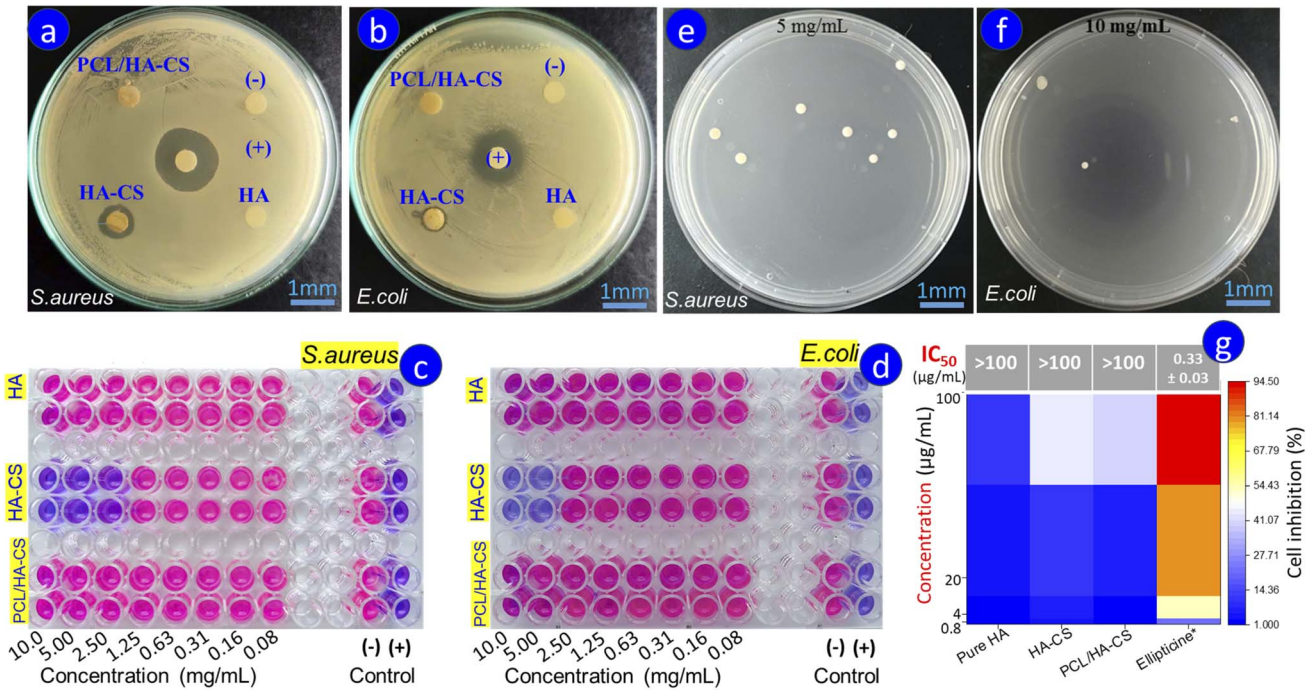

Fig. 6 Antibacterial activity of the tested samples: (a and b) agar disk diffusion assay against *S. aureus* and *E. coli*, respectively; (c and d) MIC values and (e and f) MBC values for *S. aureus* and *E. coli*, respectively; (g) percentage of inhibition on HFF cells after 48 h exposure to different concentrations of HA, HA–CS, and PCL/HA–CS (80 : 20) composites. *Control: ellipticine at a concentration 10 times lower than the test samples.

Gram-positive (*S. aureus*) and Gram-negative (*E. coli*) strains using the agar disk diffusion method and MIC/MBC evaluations (Fig. 6). Clear zones of inhibition around the samples indicated bacterial growth suppression, with the inhibition zone diameter reflecting the degree of antibacterial efficacy.

The results demonstrated that pure HA exhibited negligible antibacterial activity, as no inhibition zones were observed against either bacterial strain. This finding is consistent with previous reports confirming that HA, while biocompatible and osteoconductive, lacks intrinsic antibacterial properties.[57,58] In contrast, HA–CS composites generated distinct inhibition zones of 5.83 ± 0.24 mm against *S. aureus* and 1.93 ± 0.09 mm against *E. coli*, confirming the contribution of CS to the antibacterial response (Fig. 6a). The stronger effect against Gram-positive bacteria aligns with the known mechanism of CS, whereby positively charged amino groups interact with negatively charged bacterial membranes, leading to membrane disruption and leakage of intracellular contents.[59]

Interestingly, the PCL/HA–CS scaffolds did not produce significant inhibition zones, resembling the behavior of pure HA. This reduction in antibacterial effect can be attributed to the hydrophobic nature of the PCL matrix, which encapsulates CS and restricts its direct interaction with bacterial membranes or its diffusion into the surrounding medium. The MIC determination of the synthesized composites further confirmed this finding and was completely consistent with the results obtained above. Specifically, HA as well as PCL/HA–CS showed no inhibitory effect on either *E. coli* or *S. aureus* across the tested concentration range of 0.8–10 mg mL^{-1} (Fig. 6a and b). In contrast, HA–CS exhibited clear antibacterial activity, with a stronger inhibitory effect against *S. aureus* than *E. coli*: the MIC values were 2.5 mg mL^{-1} and 5 mg mL^{-1}, respectively. The MBC results further supported this trend. HA–CS required 10 mg mL^{-1} to achieve bactericidal activity against *E. coli*, whereas only 5 mg mL^{-1} was sufficient to completely eliminate *S. aureus* (Fig. 6e and f). A lack of inhibitory or bactericidal activity of PCL/HA–CS was likewise observed in the study conducted by Farasati Far *et al.*,[56] who showed that while CS-collagen hydrogels possessed inherent antibacterial activity, the incorporation of increasing amounts of PCL gradually diminished this effect. Specifically, samples with higher PCL content exhibited negligible antibacterial activity due to reduced surface porosity and limited exposure of CS functional groups. These findings corroborate our results, emphasizing that although PCL improves scaffold mechanical integrity, its presence can hinder the antibacterial potential of CS by altering surface properties and limiting bioactive group availability. Therefore, strategies such as surface modification, controlled CS release, or incorporation of additional antibacterial agents (*e.g.*, silver, zinc, or copper ions)[57] could be explored in future work to optimize the balance between mechanical performance and antibacterial efficacy.

The reduction of the antibacterial activity of PCL in the targeted composite is not necessarily undesirable, as it may also lower its cytotoxicity in clinical applications. The results of cytotoxicity evaluation further corroborate the antimicrobial findings described above. Cytotoxicity testing is a critical prerequisite to determine the biosafety of candidate scaffold

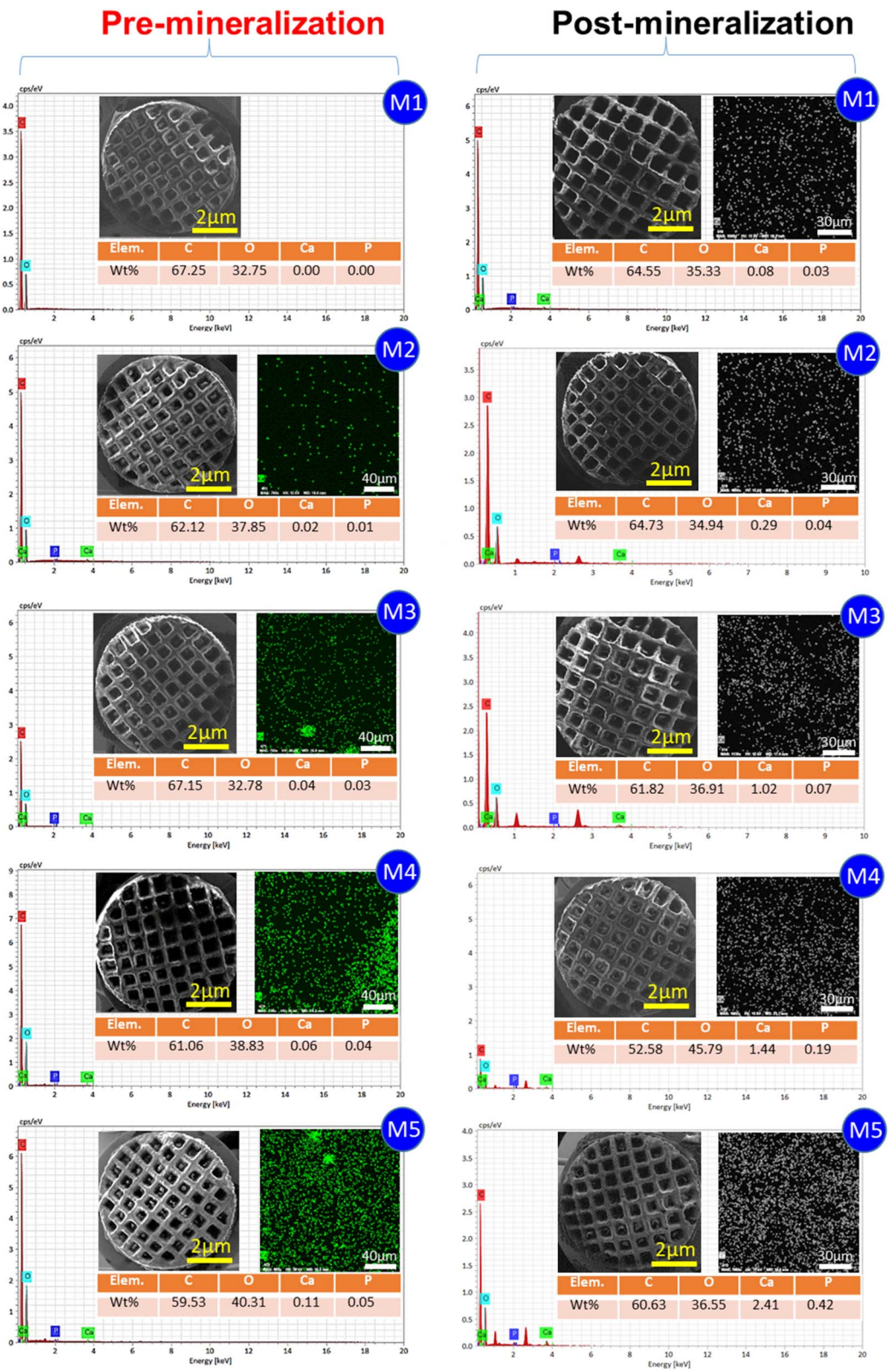

Fig. 7 SEM images, elemental compositions, and their distribution maps of PCL/HA–CS scaffolds with different PCL-to-HA–CS weight ratios before and after *in vitro* mineralization in SBF solution.

materials prior to biomedical applications. In this study, HFFs were used as a representative cell line to evaluate the cytotoxic response of HA, HA–CS, and PCL/HA–CS (80 : 20) composites after 48 h exposure at various concentrations. A summary of the cytotoxicity evaluation is presented in Fig. 6. Accordingly, at the highest concentration tested (100 μg mL^{-1}), pure HA exhibited

minimal inhibitory effects on HFF proliferation (10.41 ± 1.02%), confirming its excellent cytocompatibility. By contrast, HA–CS and PCL/HA–CS induced higher levels of growth inhibition (44.98 ± 2.52% and 42.41 ± 2.16%, respectively). Nevertheless, all three samples displayed IC_{50} values exceeding 100 μg mL^{-1}, which classifies them as non-cytotoxic according to the NCI criteria.[60] Ellipticine, used as a positive control, yielded an IC_{50} of 0.33 ± 0.03 μg mL^{-1}, confirming the robustness of the assay. The slightly increased inhibition observed for HA–CS and PCL/HA–CS may be attributed to enhanced surface interactions, partial release of CS-derived cationic groups, or polymer-related effects, which are known to transiently affect fibroblast activity without inducing cell death.[60–62] Importantly, the observed inhibition levels did not compromise overall cell viability, confirming that these materials maintain high biocompatibility. At lower concentrations (0.8–20 μg mL^{-1}), all materials showed negligible inhibitory effects, with HA–CS still exhibiting the highest value (10.91 ± 0.99 inhibition), suggesting that any potential cytotoxic interactions are concentration-dependent and remain within a safe threshold. Data clearly indicate that encapsulation of HA–CS with PCL, which limits its direct interaction, markedly reduced the toxicity of HA–CS toward HFF cells. Taken together, these findings demonstrate that HA–CS and PCL/HA–CS composites derived from crab shells exhibit favorable cytocompatibility profiles, supporting their suitability for further development as bone tissue engineering scaffolds.

3.5 *In vitro* evaluation of mineralization ability of PCL/HA–CS composite

Subsequent to the confirmation of the physicochemical and biochemical properties of HA–CS reinforced PCL composite, the

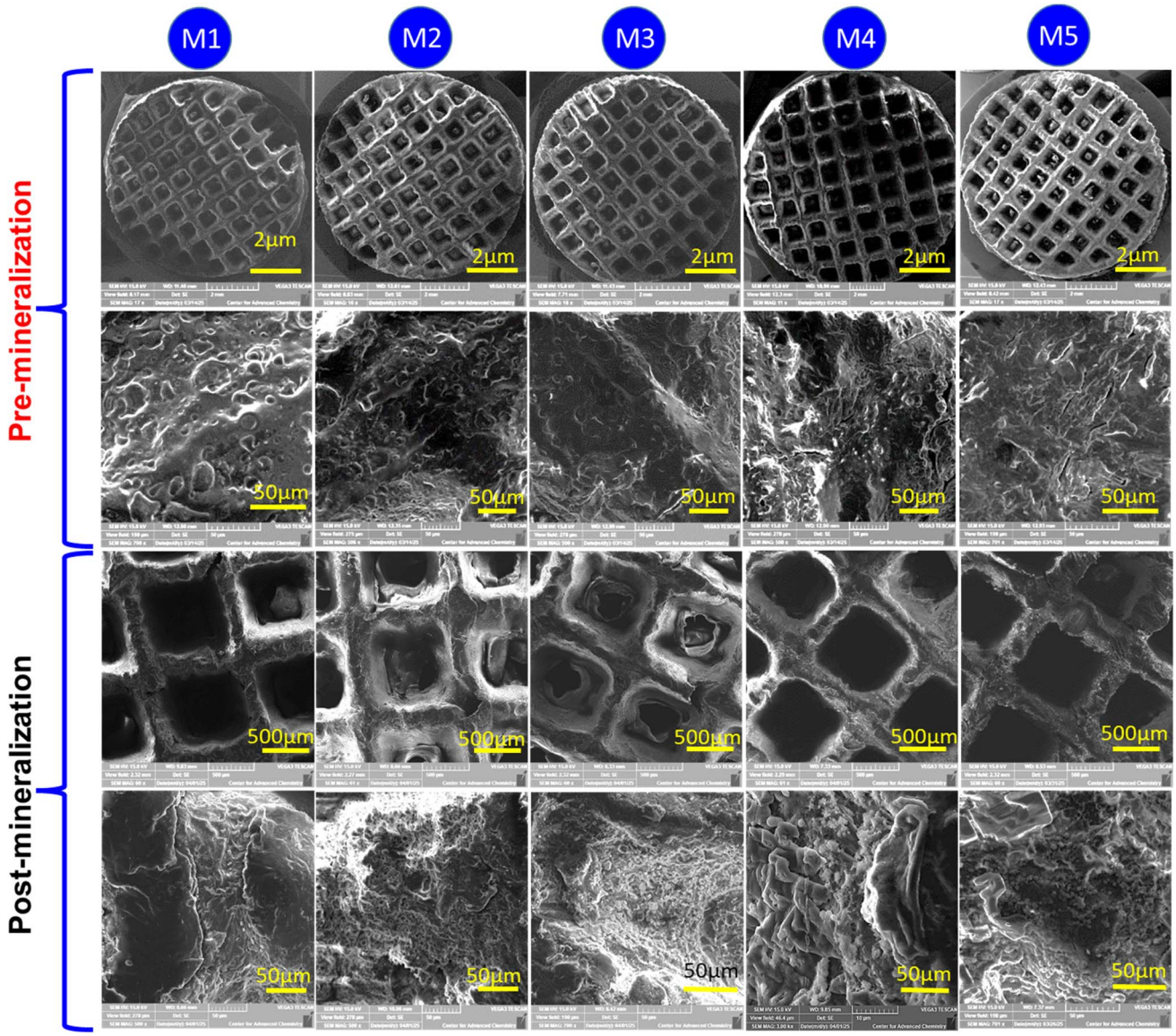

Fig. 8 SEM images at varying magnifications of PCL/HA–CS scaffolds with different PCL-to-HA–CS ratios before and after *in vitro* mineralization in SBF.

next step involved evaluating their *in vitro* mineralization behavior to assess bioactivity. The PCL/HA–CS scaffolds (circular mesh, 10 mm × 1 mm) were immersed in SBF at 37 °C for predetermined periods of 14 days. The mineralization ability of scaffolds in SBF is a key indicator of their potential to induce biomineral formation analogous to natural bone, particularly HA—the principal inorganic component of bone tissue. SBF is a biomimetic solution that replicates the ionic composition of human plasma, containing Ca^{2+}, PO_4^{3-}, Na^+, and Cl^- ions. Upon immersion in SBF, these ions adsorb and nucleate on the scaffold surface, leading to the formation of HA crystals. Morphology and surface characteristics of PCL/HA–CS scaffolds before and after *in vitro* mineralization test are presented in Fig. 7 and 8, respectively.

It is evident that prior to mineralization, the scaffold surface of PCL/HA–CS is relatively smooth, lacking the grain-like or clustered crystal structures characteristic of apatite. As the content of HA–CS increases, shallow grooves and fine ripples become more pronounced, suggesting a more homogeneous distribution of this composition. The EDS data and elemental mapping results further confirm this trend, showing that the elemental composition of Ca on the surface of PCL/HA–CS scaffolds increases proportionally with the addition of HA–CS. Additionally, this element exhibits a highly uniform distribution across the surface, consistent with the previously described results of water uptake and biodegradation analyses of the resultant composite. Despite the confirmation of Ca presence through EDS and element mapping analyses, the morphology of the pure PCL scaffold remained unchanged following 14 days of mineralization in SBF. This is reasonable, as PCL is an inert polymer and does not provide nucleation sites for HA crystallization. Conversely, on the surface of PCL/HA–CS samples, numerous particle clusters and spherical crystals with cauliflower-like morphology emerged across the scaffold. The particles exhibited heterogeneous sizes and shapes, characteristic of HA or calcium phosphate formed in SBF. Increasing the HA–CS content resulted in a higher particle density and larger crystal size, for sample M5 containing 40%HA–CS, the surface Ca content reached an average of 2.41%, representing an approximate 22-fold increase compared to the value prior to the mineralization process.

Of particular note is that some agglomerations of HA on the composite surface (as illustrated by the elemental map in Fig. 7) completely disappeared after mineralization. This observation suggests that the mineralization process of PCL/HA–CS proceeded *via* a dissolution–reprecipitation mechanism, as previously reported.[63,64] In this pathway, partial dissolution of HA or the release of Ca^{2+} and PO_4^{3-} ions into the SBF solution increases the local ionic concentration near the material surface, subsequently promoting re-deposition and the growth of a secondary apatite layer. This newly formed layer not only develops on pre-existing HA regions but also uniformly covers the entire surface, facilitated by the –OH and $–NH_2$ groups of CS and other active sites. Consequently, a more homogeneous apatite layer is produced, no longer governed by the initial HA distribution, as evidenced in the obtained elemental mapping images. The obtained results indicate that the PCL scaffold incorporating HA–CS possesses a clear apatite-forming ability and can promote surface mineralization under SBF condition.

4 Conclusion

This study demonstrates that the valorization of crab shells into an HA–CS composite, followed by blending with PCL, provides a sustainable and effective strategy for developing scaffolds for bone tissue regeneration. The obtained HA–CS composite contained 78.37% HA, and incorporating up to 40% HA–CS into the PCL matrix yielded an optimal balance between mechanical strength and biodegradability. By tuning the HA–CS content, the degradation rate of the PCL/HA–CS scaffolds during the first four weeks can be precisely controlled, enabling better synchronization between scaffold resorption and new bone formation. Our results also reveal that HA in the scaffold functions not merely as a passive inorganic filler but as an active ion reservoir that promotes the development of a uniformly distributed Ca–P-rich apatite layer. While these findings highlight the potential of the PCL/HA–CS scaffolds for bone regeneration, the current work is limited to *in vitro* evaluations. Future *in vivo* studies and long-term assessments will be essential to fully validate their translational potential for clinical application.

Conflicts of interest

The authors declare that they have no known competing financial interests or personal relationships that could have appeared to influence the work reported in this paper.

Data availability

The authors confirm that the data supporting the study findings are available within the manuscript. Raw data that support these findings are available from the corresponding author, upon request.

References

1 A. H. Hoveidaei, M. Sadat-Shojai, S. S. Nabavizadeh, R. Niakan, A. Shirinezhad, S. MosalamiAghili and S. Tabaie, *Bone*, 2025, **192**, 117363.
2 C. Liu, M. Xu, Y. Wang, Q. Yin, J. Hu, H. Chen, Z. Sun, C. Liu, X. Li, W. Zhou and H. Liu, *Mater. Sci. Eng., R*, 2024, **161**, 100870.
3 A. Vijayan, J. Vishnu, R. A, B. Shankar and S. Sambhudevan, *Biomater. Sci.*, 2025, **13**, 913–945.
4 A. Bushra, A. Subhani and N. Islam, *Compos., Part C: Open Access*, 2023, **12**, 100402.
5 H. Wang, R. Sun, S. Huang, H. Wu and D. Zhang, *Heliyon*, 2024, **10**, e25832.
6 M. R. Gal, M. Rahmaninia and M. A. Hubbe, *Carbohydr. Polym.*, 2023, **309**, 120665.
7 Y.-P. Guo, J.-J. Guan, J. Yang, Y. Wang, C.-Q. Zhang and Q.-F. Ke, *J. Mater. Chem. B*, 2015, **3**, 4679–4689.

8 M. S. Gaafar, S. M. Yakout, Y. F. Barakat and W. Sharmoukh, *RSC Adv.*, 2022, **12**, 27564–27581.
9 Y. Wibisono, S. R. Ummah, M. B. Hermanto, G. Djoyowasito and A. Noviyanto, *Results Eng.*, 2024, **21**, 101781.
10 D. F. Fitriyana, R. Ismail, A. P. Bayuseno, J. P. Siregar and T. Cionita, *J. Renewable Mater.*, 2024, **12**, 1145–1163.
11 Z. U. Arif, M. Y. Khalid, R. Noroozi, A. Sadeghianmaryan, M. Jalalvand and M. Hossain, *Int. J. Biol. Macromol.*, 2022, **218**, 930–968.
12 A. Chanda, J. Adhikari, A. Ghosh, S. R. Chowdhury, S. Thomas, P. Datta and P. Saha, *Int. J. Biol. Macromol.*, 2018, **116**, 774–785.
13 H. Yu, L. Xia, X. Leng, Y. Chen, L. Zhang, X. Ni, J. Luo and W. Leng, *Front. Bioeng. Biotechnol.*, 2022, **10**, 01–11.
14 F. Scalera, S. I. A. Pereira, A. Bucciarelli, D. M. Tobaldi, A. Quarta, F. Gervaso, P. M. L. Castro, A. Polini and C. Piccirillo, *Mater. Today Sustain.*, 2023, **21**, 100334.
15 H. Wang, R. Sun, S. Huang, H. Wu and D. Zhang, *Heliyon*, 2024, **10**, e25832.
16 M. Shakir, S. Mirza, R. Jolly, A. Rauf and M. Owais, *New J. Chem.*, 2018, **42**, 363–371.
17 N. Topić Popović, V. Lorencin, I. Strunjak-Perović and R. Čož-Rakovac, *Appl. Sci.*, 2023, **13**, 623.
18 J. N. Murphy and F. M. Kerton, in *Fuels, Chemicals and Materials from the Oceans and Aquatic Sources*, Wiley, 2017, pp. 189–227.
19 E. O. Ningrum, M. A. Nugroho, T. Gotoh, A. D. Karisma, T. S. E. Perwitasari, A. Hamzah, S. Z. Abidin, A. Ajit and S. Widiyanto, *J. Chem. Technol. Biotechnol.*, 2025, **100**, 2638–2649.
20 A. Tapia, R. Seña, H. Zambrano and V. Paredes, *Int. J. Biol. Macromol.*, 2025, **320**, 145963.
21 Z. Liu, J. Shi, L. Chen, X. He, Y. Weng, X. Zhang, D.-P. Yang and H. Yu, *Int. J. Biol. Macromol.*, 2024, **274**, 133172.
22 H.-C. Hsu, Y.-C. Chung, S.-C. Wu, Y.-C. Ho, H.-H. Chang and W.-F. Ho, *Surf. Coating. Technol.*, 2022, **437**, 128364.
23 T. Kokubo and H. Takadama, *Biomaterials*, 2006, **27**, 2907–2915.
24 H. C. Hsu, S. C. Wu, C. Y. Lin and W. F. Ho, *Coatings*, 2023, **13**, 228.
25 S. Swamiappan, X. Xie, C. Lu and X. Peng, *Ceram. Int.*, 2025, **51**, 20452–20464.
26 J. Kumirska, M. Czerwicka, Z. Kaczyński, A. Bychowska, K. Brzozowski, J. Thöming and P. Stepnowski, *Mar. Drugs*, 2010, **8**, 1567–1636.
27 A. T. Paulino, J. I. Simionato, J. C. Garcia and J. Nozaki, *Carbohydr. Polym.*, 2006, **64**, 98–103.
28 M. Gurumendi, F. López, L. J. Borrero-González, T. Terencio, M. Caetano, C. Reinoso and G. González, *ACS Omega*, 2023, **8**, 13763–13774.
29 I. C. G. Sousa, S. C. Teixeira, M. V. de Souza, M. B. M. Conde, G. R. Bailon, S. H. S. Cardoso, L. D. Araújo, E. B. de Oliveira, S. O. Ferreira, T. V. de Oliveira and N. de F. F. Soares, *Foods*, 2025, **14**, 2785.
30 S. Yasmeen, M. Kabiraz, B. Saha, M. Qadir, M. Gafur and S. Masum, *Int. Res. J. Pure Appl. Chem.*, 2016, **10**, 1–14.
31 H. Abriyanto, H. Susanto, T. Maharani, A. M. I. Filardli, R. Desiriani and N. Aryanti, *ACS Omega*, 2022, **7**, 46066–46078.
32 J. F. Leal, P. S. M. Amado, J. P. Lourenço and M. L. S. Cristiano, *Toxins*, 2024, **16**, 200.
33 A. Saravanan and R. P. Ramasamy, *J. Polym. Res.*, 2016, **23**, 174.
34 S. Knop, T. L. C. Jansen, J. Lindner and P. Vöhringer, *Phys. Chem. Chem. Phys.*, 2011, **13**, 4641.
35 M. Gurumendi, F. López, L. J. Borrero-González, T. Terencio, M. Caetano, C. Reinoso and G. González, *ACS Omega*, 2023, **8**, 13763–13774.
36 D. N. Iqbal, Z. Tariq, B. Philips, A. Sadiqa, M. Ahmad, K. M. Al-Ahmary, I. Ali and M. Ahmed, *RSC Adv.*, 2024, **14**, 8652–8664.
37 N. G. Madian, B. A. El-Ashmanty and H. K. Abdel-Rahim, *Polymers*, 2023, **15**, 2587.
38 T. Martínez Rodríguez, C. Valentino, F. R. Rodríguez Pozo, P. Hernández Benavides, F. Arrebola Vargas, J. M. Paredes, C. I. Sainz-Díaz, G. R. Iglesias, S. Rossi, G. Sandri, M. del M. Medina Pérez and C. Aguzzi, *J. Funct. Biomater.*, 2024, **15**, 69.
39 J. Becerra, M. Rodriguez, D. Leal, K. Noris-Suarez and G. Gonzalez, *J. Mater. Sci. Mater. Med.*, 2022, **33**, 18.
40 C. H. Ünlü, E. Pollet and L. Avérous, *Int. J. Mol. Sci.*, 2018, **19**, 3799.
41 P. Ranjane, M. Deshpande and P. S. Kulkarni, *J. Appl. Polym. Sci.*, 2023, **140**, 54533.
42 Q. Li, Y. Qian, M. Xing and B. Li, *Sep. Purif. Technol.*, 2025, **361**, 131207.
43 S. Bandara, C. Carnegie, C. Johnson, F. Akindoju, E. Williams, J. M. Swaby, A. Oki and L. E. Carson, *Heliyon*, 2018, **4**, e00737.
44 K. Yoshida, S. Teramoto, J. Gong, Y. Kobayashi and H. Ito, *Polymers*, 2024, **16**, 1830.
45 J. Kozak and A. Townshend, in *Reference Module in Chemistry, Molecular Sciences and Chemical Engineering*, ed. M. M. Paul Worsfold, C. Poole and A. Townshend, Elsevier, 3rd edn., 2019, pp. 111–120.
46 Z. Zhang, G. Yang, M. He, L. Qi, X. Li and J. Chen, *Int. J. Mol. Sci.*, 2022, **23**, 15345.
47 H. Jinnai, *Microscopy*, 2022, **71**, i148–i164.
48 F. Wang, Y. Wu and B. Nestler, *Adv. Mater.*, 2023, **35**, 202210745.
49 X. Feng, H. Xu, L. Bai, J. Yang, W. Yang and Y. Hu, *Int. J. Biol. Macromol.*, 2025, **329**, 147615.
50 C. Shuai, J. Zan, F. Deng, Y. Yang, S. Peng and Z. Zhao, *ACS Sustain. Chem. Eng.*, 2021, **9**, 1814–1825.
51 N. Abdian, M. Etminanfar, H. Hamishehkar and S. O. R. Sheykholeslami, *Int. J. Biol. Macromol.*, 2024, **260**, 129565.
52 A. Rahman, K. F. Tanvir, H. K. Jui, M. T. Ahmed, S. M. A. Nipu and S. Bin Hussain, *Results Eng.*, 2025, **27**, 106156.
53 X. Zhou, J. Chen, H. Sun, F. Wang, Y. Wang, Z. Zhang, W. Teng, Y. Ye, D. Huang, W. Zhang, X. Mo, A. Liu, P. Lin,

Y. Wu, H. Tao, X. Yu and Z. Ye, *J. Nanobiotechnol.*, 2021, **19**, 420.
54 Q. Dong, M. Zhang, X. Zhou, Y. Shao, J. Li, L. Wang, C. Chu, F. Xue, Q. Yao and J. Bai, *Mater. Sci. Eng., C*, 2021, **129**, 112372.
55 L. Lu, Q. Zhang, D. M. Wootton, R. Chiou, D. Li, B. Lu, P. I. Lelkes and J. Zhou, *J. Appl. Biomater. Funct. Mater.*, 2014, **12**, 145–154.
56 B. Farasati Far, M. R. Naimi-Jamal, M. Jahanbakhshi, H. Rostamani, M. Karimi and S. Keihankhadiv, *Int. J. Biol. Macromol.*, 2023, **253**, 127448.
57 M. Abbasi, M. Rashnavadi, M. Gholami and S. Molaei, *Sci. Rep.*, 2025, **15**, 12101.
58 V. D. Doan, H. Y. Hoang, T. T. T. Nguyen, B. D. Mai, V. A. Tran and V. T. Le, *Ceram. Int.*, 2025, **51**, 48889–48902.
59 R. Antil, J. Lathwal, S. S. Gulia and S. Ahmed, in *Advanced Applications of Biobased Materials*, Elsevier, 2023, pp. 363–378.
60 I. Canga, P. Vita, A. I. Oliveira, M. Á. Castro and C. Pinho, *Molecules*, 2022, **27**, 4989.
61 B. Y. S. Kumar, A. M. Isloor, G. C. M. Kumar, Inamuddin and A. M. Asiri, *Sci. Rep.*, 2019, **9**, 15957.
62 D. Frumento and Ș. Țălu, *J. Compos. Sci.*, 2025, **9**, 305.
63 T. D. Pham, T. T. Bui, T. T. Trang Truong, T. H. Hoang, T. S. Le, V. D. Duong, A. Yamaguchi, M. Kobayashi and Y. Adachi, *J. Mol. Liq.*, 2020, **298**, 111981.
64 T. Kokubo and S. Yamaguchi, *J. Biomed. Mater. Res., Part A*, 2019, **107**, 968–977.